Role of Graphene on Hierarchical Flower-like NiAl Layered Double Hydroxide-Nickel foam-Graphene as Binder-free Electrode for High-rate Hybrid Supercapacitor

Luojiang Zhang [a], K.N. Hui [b,*] K.S. Hui [a,**], Xin Chen [a], Rui Chen [c], Haiwon Lee [c]

[a] Department of Mechanical Convergence Engineering, Hanyang University, 17 Haengdang-dong, Seongdong-gu, Seoul 133-791, Republic of Korea

[b] Institute of Applied Physics and Materials Engineering, University of Macau, Avenida da Universidade, Taipa, Macau

[c] Department of Chemistry, Hanyang University, 17 Haengdang-dong, Seongdong-gu, Seoul 133-791, Republic of Korea

[*] Corresponding author. Fax: +853 8822-2426; Tel: +853 8822-4422; bizhui@umac.mo (K.N. Hui)

[**] Corresponding author. Fax: +82-2-2220-2299; Tel: +82-2-2220-0441; kshui@hanyang.ac.kr (K.S. Hui)

Abstract: In this work, a facile two-step hydrothermal method was reported to grow hierarchical flower-like NiAl layered double hydroxide (LDH) directly on 3D nickel foam (NF) which was further coated with 2D graphene nanosheets (GNS) layers as binder-free supercapacitor electrode. The positive and negative effects of GNS on the electrochemical performance of LDH-NF electrode were investigated in detail. The prepared LDH-NF/GNS electrode maintained an enhanced specific capacity of 165.6 C g^{-1} after 4000 cycles at a high current density of 40 A g^{-1}. Furthermore, a hybrid supercapacitor, with LDH-NF/GNS and GNS-NF as the positive and negative electrodes, achieved an energy density (31.5 Wh kg^{-1} at a power density of 400 W kg^{-1}) and super long-term cycle stability (a specific capacity of 67.2 C g^{-1} at 5 A g^{-1} after 5000 cycles with 80% retention). This study not only opens up the possibility of engineering LDH-NF/GNS into a promising electrode, but also highlights the positive and negative roles of GNS on LDH-NF as binder-free electrodes for further development of high-performance supercapacitors.

Keywords: Hybrid supercapacitor; Layered double hydroxide; Nickel foam; Graphene; Energy density

Introduction

The ever-increasing energy needs and the limited availability of fossil fuels has led to the development of high-performance energy storage systems, such as batteries [1], fuel cells [2] and supercapacitors (SCs) [3]. SCs have attracted considerable interest over the past few decades owing to their fast charge and discharge rate, high power density, long cycle life, and high reliability [4-7]. Generally, SCs can be divided into electrical double layer capacitors (EDLCs) where the double layer is charged and pseudocapacitors where reversible redox reactions proceed [8-9]. Currently, EDLCs exhibit high power density, but suffer from low energy density; while pseudocapacitors possess a higher specific capacitance of 10-100 times than that of EDLCs, but encounter unstable cycle performance [10-14]. Therefore, the design and synthesis of new electrode materials with improved electrochemical and physical properties are the important factors in leading to high energy density and power density for supercapacitors [15].

As promising positive electrode materials, layered double hydroxides (LDH), which normally have the general formula $[M^{II}_{1-x}M^{III}_x(OH)_2]^{x+}[A^{n-}]_{x/n} \cdot mH_2O$, where M^{II} and M^{III} denote the layers of divalent and trivalent metallic ions, respectively, and A^{n-} is an interlayer anion, have attracted increasing interest because of their relatively low cost, high redox activity, and environmentally friendly nature [16-18]. However, owing to the high similarity of LDH based battery-type materials to pseudocapacitive materials in terms of the charge storage mechanism and high power performance, these kinds of electrode materials once were mistaken for pseudocapacitive materials [19-21]. For example, hierarchical NiAl-LDH powders fabricated via a solvothermal approach exhibited specific capacitances of 814 F g^{-1} at 2 A g^{-1} and 409 F g^{-1} at 18 A g^{-1}, respectively [22]. Shao et al. [23] developed hollow NiAl-LDH microspheres, showing a specific capacitance of 735 F g^{-1} at 2 A g^{-1} and good cycle performance. On the other hand, for applications to SCs, these LDH

1   powdery materials [19, 22-23], should be mixed with a conducting agent and binder and then coated on

2   nickel foam (NF) as electrodes. This method, however, has the following drawbacks [24]: (1) it is

3   difficult to make a homogeneous paste, (2) the troublesome preparation steps have a great

4   influence on the electrochemical performance, and (3) the contact and electrical conductivity

5   between the LDH and NF are poor. The limited electrochemical performance is also due to the

6   low conductivity and the highly packed morphology of the LDH materials [25]. As a result, their

7   electrochemical behavior is insufficient to meet the demands of new energy storage devices. To

8   solve these problems, one effective method is to grow LDH with interconnected architecture

9   directly on a conductive substrate to form a binder-free electrode [21]. NF, with a desirable 3D open-

10   porous structure, high specific surface area and excellent physical strength [26-27], can be a promising

11   substrate in LDH-based SCs, because of the following advantages [28-30]: (1) it can reduce the severe

12   agglomeration of LDH, allowing maximum use of the active materials, (2) the 3D porous NF

13   provides more channels to facilitate fast penetration of the electrolyte ions into the active LDH

14   materials of electrodes, and (3) compared to the common slurry-coating technology, the direct

15   contact of LDH on NF avoids the use of polymer binder/conductive additives, and reduces "dead

16   volume" substantially in SCs electrodes. For example, NiAl-LDH/NF [24, 31] exhibited higher

17   specific capacitance and better high-rate performance (0.5-10 A g^{-1}) than the conventional NiAl-

18   LDH powder-based electrodes. However, in these papers [24, 31], the high-rate performance of the

19   electrodes (>10 A g^{-1}) and the morphological stability of NiAl-LDH on NF after the cycling tests

20   were not investigated, which are important for understanding the limitations of LDH-NF for high-

21   performance SCs devices.

22   Considerable work has shown that the electrochemical nature of powdery graphene-based LDH

23   composites would be enhanced greatly [19, 32-34]. Graphene nanosheets (GNS), a single layer of

carbon atoms with a two dimensional structure, have attracted extensive interest worldwide owing

to their highly accessible surface area, good electrical conductivity, chemical stability and

mechanical strength [35-37]. First, the existence of GNS in a composite can provide a conducting

support to promote the rapid Faradaic charging and discharging of LDH [20]. Second, GNS can form

an open structure to improve the connection between LDH and the electrolyte, which can fully

utilize the active LDH during the charging and discharging process [19]. Third, the flexible GNS can

efficiently buffer the volume change in LDH during a long cycling process [19]. However, there are

no reports of the role of GNS on the electrochemical performance and the stability of binder-free

LDH-NF electrodes at a high current density, which will be important for the future development

of graphene-LDH/NF-based electrodes for high-performance SCs.

Inspired by the above findings, this paper reports a facile and effective method for loading GNS

layers on the surface of hierarchical NiAl-LDH grown directly on NF (LDH-NF) as binder-free

SCs electrode, LDH-NF/GNS. The effects of GNS (both positive and negative) on the

electrochemical capacity and the stability of the LDH-NF electrode was elucidated in detail by

cyclic voltammetry (CV), galvanostatic charge-discharge measurements and electrochemical

impedance spectroscopy (EIS). Unlike the positive role of GNS in powdery LDH-based

composites, the deposition of GNS on a LDH-NF electrode partially blocked the active LDH for

an effective Faradaic reaction. The results indicated that the LDH-NF/GNS electrode exhibited

inferior performance with a specific capacity of 645.6 C g^{-1} at 2 A g^{-1} and 209.8 C g^{-1} at 40 A g^{-1},

respectively, compared to those of the LDH-NF electrode (817.7 C g^{-1} at 2 A g^{-1} and 415.4 C g^{-1}

at 40 A g^{-1}). However, the cycling performance of the LDH-NF/GNS electrode was 54.1% at 40

A g^{-1} after 4000 cycles compared to the LDH-NF electrode (a retention of 45.9%), indicating the

beneficial role of GNS on a binder-free LDH-NF electrode. Moreover, a hybrid supercapacitor

(HSC) was fabricated with LDH-NF/GNS as the positive electrode and GNS coated on NF (GNS-NF) as the negative electrode, which exhibited an energy density of 31.5 Wh kg^{-1} at a power density of 400 W kg^{-1} and showed good cycling stability with 80% retention after 5000 cycles at 5 A g^{-1}. This work highlighted the positive and negative roles of GNS on binder-free LDH-NF electrodes for high-performance supercapacitors.

Experimental Section

Materials preparation

Fabrication of the LDH-NF electrode

Analytical-grade chemicals ($Ni(NO_3)_2 \cdot 6H_2O$, $Al(NO_3)_3 \cdot 9H_2O$, and urea) and NF were used. A piece of NF (10×10×1 mm, 110 PPI, 31 mg cm^{-2}) was degreased with 6.0 mol L^{-1} HCl for 15 min, rinsed with water, and dried at 50 °C in an oven for 12 h. A total of 9 mmol of $Ni(NO_3)_2 \cdot 6H_2O$ and 3 mmol of $Al(NO_3)_3 \cdot 9H_2O$ were dissolved in a solution containing 75 mL of H_2O and 40 mmol of urea. The solution was stirred magnetically for 20 min in air at room temperature and transferred to a 100 mL-autoclave vessel. The NF was then immersed in the solution and heated to 140 °C for 10 h. The NF covered with the LDH nanosheets, was washed with H_2O and ethanol to remove surface ions using an ultrasonic bath cleaner, and dried at 60 °C for 12 h to remove the adsorbed solvents. The NiAl-LDH loading on NF was approximately 5 mg and the obtained electrode was labeled LDH-NF.

Fabrication of the LDH-NF/GNS electrode

GO was prepared from the graphite powder (SP, Sinopharm Chemical Reagent Co. Ltd) using a modification of Hummers' method [19]. In a typical procedure, 30 mg GO was suspended in 60 mL H_2O with ultrasonication for 1 h and transferred to a 100 mL- autoclave vessel. The as-synthesized LDH-NF electrode was immersed in the GO suspension for 3 h and heated to 160 °C for 3 h. The

1   as-prepared sample was washed with H_2O and ethanol to remove the surface ions using an

2   ultrasonic bath cleaner, and then dried at 60 °C for 12 h to remove the adsorbed solvents. The GNS

3   loading on LDH-NF was approximately 1.7 mg and the obtained electrode was labelled LDH-

4   NF/GNS.

5   *Fabrication of the GNS-NF electrode*

6   30 mg GO was suspended in 60 mL H_2O with ultrasonication for 1 h to obtain a homogeneous GO

7   aqueous dispersion. The GO dispersion was sealed in a 100 mL- autoclave vessel and maintained

8   at 180 °C for 3 h. After the 0autoclave was cooled to room temperature, the resulting black

9   precipitate was centrifuged and washed sequentially with H_2O and ethanol, and then dried at 60 °C

10   for 12 h to obtain the GNS powder. GNS electrodes were fabricated using the following method:

11   a mixture of GNS, 10 wt.% of acetylene black, 10 wt.% of polytetrafluoroethylene and a small

12   amount of water was prepared by milling to produce a homogeneous paste. After coating the above

13   paste on NF (10×10×1 mm), the electrodes were dried at 50 °C for 12 h before pressing under a

14   pressure of 20 MPa.

15   **Materials characterization**

16   X-ray diffraction (XRD, Bruker D8 Advance X-ray) of the samples was performed using Cu Kα

17   radiation (λ = 0.15406 nm) at 40 kV and 30 mA. The scanning speed was 5° min^{-1} with a 0.02°

18   step. The morphology and the structural properties of the samples were observed by field emission

19   scanning electron microscopy (FESEM, LEO-1550) with an applied voltage of 5 kV.

20   **Electrochemical measurements**

21   The electrochemical properties of the as-obtained LDH-NF, LDH-NF/GNS and GNS single

22   electrodes were investigated under a three-electrode system with a 6 M KOH aqueous solution as

23   the electrolyte at room temperature. The LDH-NF and LDH-NF/GNS (10×10×1 mm) were used

24   directly as the working electrode. A platinum foil and a saturated calomel electrode (SCE) were

7

1 used as the counter and reference electrodes, respectively. The electrochemical properties of the

2 hybrid supercapacitor were examined under a two-electrode cell configuration with LDH-NF/GNS

3 as the positive electrode and GNS as the negative electrode in a 6 M KOH electrolyte solution. A

4 ZIVE SP2 electrochemical working station instrument was employed for cyclic voltammetry (CV),

5 galvanostatic charge/discharge measurements and electrochemical impedance spectroscopy (EIS).

6 The EIS measurements were carried out over the frequency range from 100 kHz to 0.01 Hz at the

7 open circuit potential with an ac perturbation of 5 mV. The mean of three sets of independent

8 experiments (deviations within ±5%) using three different batches of the samples are reported.

9 The specific capacity (C) of LDH-NF, LDH-NF/GNS were calculated from the

10 galvanostatic charge/discharge curves as follows: $C = I \times \Delta t / m$, where I is the discharge

11 current (A), Δt is the discharge time (s) and m is the mass of the electroactive material in

12 the electrode (g), while the specific capacitance (C_s) of GNS were calculated by $C_s =$

13 $I \times \Delta t / (m \times \Delta V)$, where I is the discharge current (A), Δt is the discharge time (s), m is the

14 mass of GNS in the electrode (g), and ΔV is the total potential deviation (V). The specific

15 capacity (C') of HSC was calculated from the galvanostatic charge/discharge curves as

16 follows: $C' = I \times \Delta t / m'$, where m' is the total mass of electroactive materials in the positive

17 and negative electrodes (g). The energy and power densities of the HSC were calculated as

18 follows: $E = 0.5 \times C' \times V$, $P = E / \Delta t$, where E (Wh kg^{-1}) is the energy density, V (V) is the

19 cell voltage excluding the IR drop, P (W kg^{-1}) is the average power density, and Δt is the
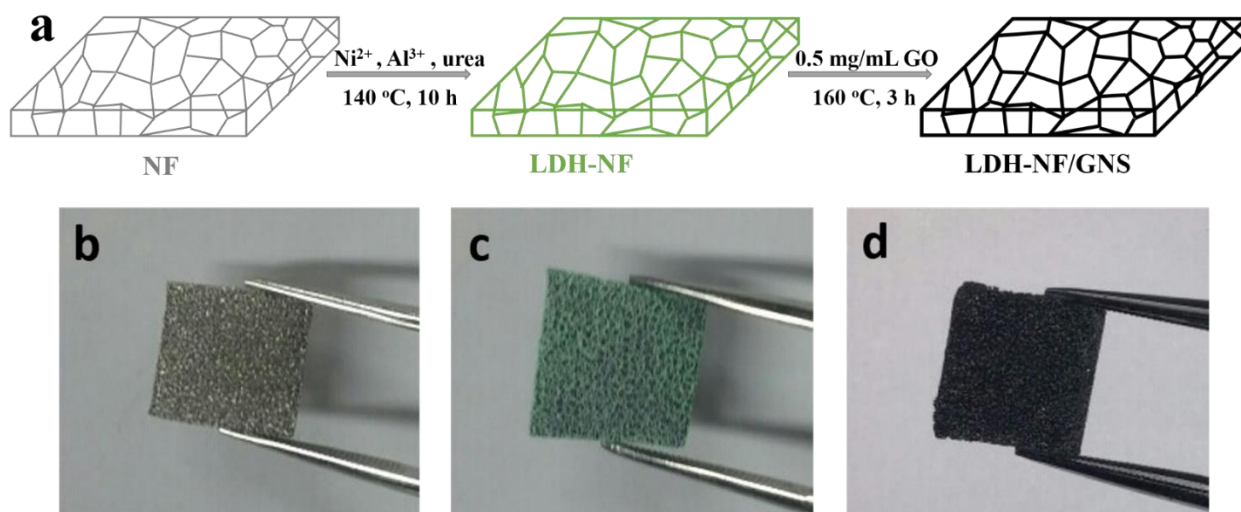
20 discharge time.

21

22 **Results and Discussion**

23 **Characterization of the samples**

24

Fig. 1 (a) Typical synthesis procedure of 3D LDH-NF/GNS electrodes. Optical image of (b) NF, (c) LDH-NF and (d) LDH-NF/GNS.

A 3D LDH-NF/GNS electrode was prepared using a simple two-step process, as illustrated in Fig. 1a, which can be scaled up easily. First, NiAl-LDH was deposited in situ on a 3D porous NF as a binder-free LDH-NF electrode. Second, a hydrothermal treatment was conducted to load GNS on the LDH-NF electrode. Briefly, a piece of cleaned NF (Fig. 1b) was immersed into a solution containing Ni^{2+}, Al^{3+} and urea, transferred to an autoclave, and maintained at 140 °C for 10 h. The process involved the transportation of metal ions (Ni^{2+}, Al^{3+}) to the NF surface, the adsorption and enrichment of the ions, and the nucleation and growth of NiAl-LDH crystals on NF. During the process, the metal ions (Ni^{2+}, Al^{3+}) reacted with CO_3^{2-} and OH^- (decomposed from the urea) to form NiAl-LDH particles [24], which were grown directly on NF as the reaction continued, and the NF was turned from gray to green due to the green colored NiAl-LDH (Fig. 1c). The material was characterized by X-ray diffraction (XRD; Supporting Information, Fig. S1a). With the exception of the peaks for NF, the XRD pattern of NiAl-LDH exhibited reflections of (003), (006), (012), (015), and (110), representing R3m symmetry and a typical hydrotalcite-like structure (JCPDS 15-

9

1   0087). In the second step, LDH-NF was then immersed in 60 mL of a graphene oxide (GO)

2   solution (0.5 mg mL^{-1}) and heated to 160 ^{o}C for 3 h. The feature XRD peak of exfoliated GO was

3   observed appeared at 10.4° (002) (Fig. S1b), corresponding to an interlayer spacing of 0.84 nm.

4   GO is hydrophilic and highly dispersible in water due to the oxygen functional groups on its basal

5   planes and edges [20]. During this process, GO sheets with lateral dimensions of several micrometers

6   (Fig. S2a), were coated tightly on the LDH surface because of the electrostatic interactions of

7   negatively charged functional groups on GO and a positively charged LDH layer [38]. Subsequently,

8   through the second hydrothermal process, GO was reduced to GNS film [39] and the green LDH-NF

9   turned black due to the coverage of black GNS (Fig. 1d). Finally, a 3D binder-free LDH-NF/GNS

10   electrode was prepared. The diffraction peaks observed in the composite (Fig. S1c) were in

11   accordance with those of LDH, although the intensities of the peaks became weaker because of

12   the poor crystallization of the LDH-NF/GNS materials, which could be attributed to the loading

13   of GNS [20].
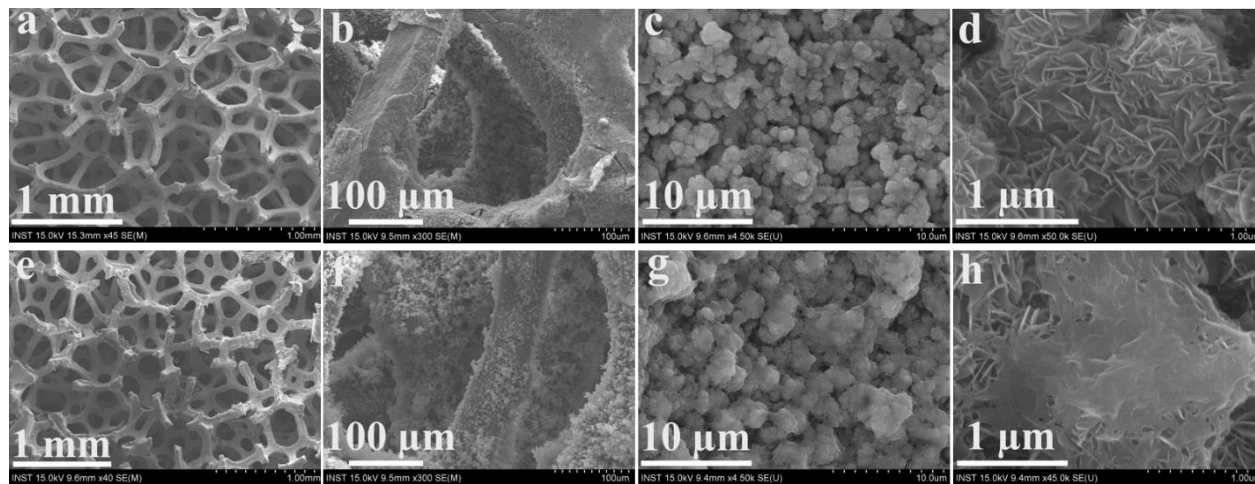

Fig. 2 SEM images of (a-d) LDH-NF and (e-h) LDH-NF/GNS.

Fig. 2 presents the structures of the LDH-NF and LDH-NF/GNS electrodes. Fig. S2b shows an

SEM image of the blank NF which has smooth surface with a 3D cross-linked macroporous

structure for providing a high specific surface area (110 PPI) to facilitate sufficient loading of LDH

10

1   materials per unit electrode area [28]. Fig. 2a-d show the typical morphology of NiAl-LDH on NF.

2   As shown in Fig. 2a, the 3D porous structure of NF was retained after the hydrothermal growth of

3   NiAl-LDH. In Fig. 2b, the NF was covered with a large number of particles, both outside and

4   inside. The results indicated that the surfaces of NF were covered completely with LDH. In Fig.

5   2c, the particles were composed of hierarchical flower-like LDH assemblies with a mean diameter

6   of 1 µm. As shown in Fig. 2d, this flower-like LDH assembly possessed an open-porous network

7   structure, which was composed of interconnected nanoplatelets with a mean thickness of 10 nm.

8   These nanoplatelets were intersected and aligned vertically on the NF, which can facilitate the

9   charge transport and ion diffusion [40]. Fig. 2e-h show the LDH-NF/GNS structures after loading

10 GNS on the LDH-NF surface. Fig. 2e and 2f show that the LDH on NF was thermodynamically

11 stable after the second hydrothermal treatment process. The LDH-NF served as a robust scaffold

12 for loading the conducting multilayered GNS, which covered the flower-like LDH assemblies to

13 form a continuous 3D conductive network (Fig. 2g-h). On the other hand, to a certain extent, the

14 open-porous network of LDH was blocked by these GNS layers. The role of GNS on the

15 electrochemical performance and the stability of the binder-free LDH-NF electrode was studied as

16 follows.

17 **Electrochemical performance of the electrodes**

18

11
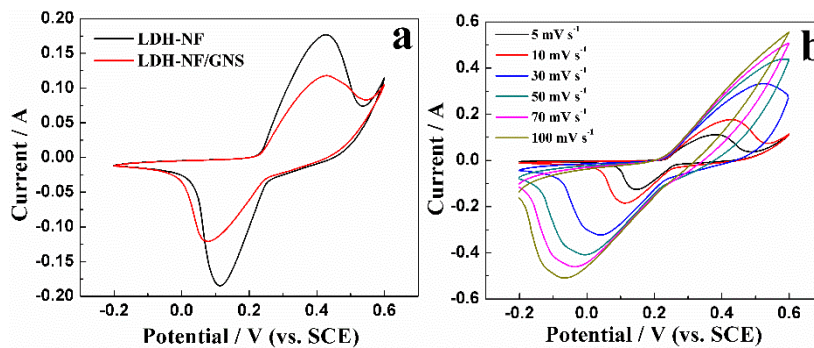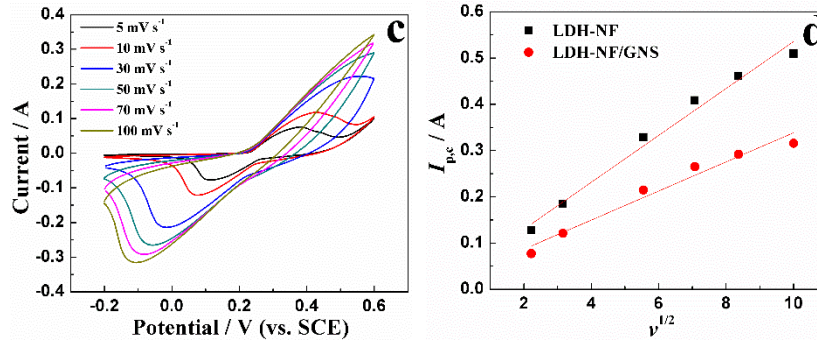
Fig. 3 (a) Comparison of LDH-NF and LDH-NF/GNS at a scan rate of 10 mV s^{-1}. CV curves of (b) LDH-NF and (c) LDH-NF/GNS at different scan rates. (d) Relationship of the cathodic peak current of LDH-NF and LDH-NF/GNS with different scan rates.

Fig. 3a shows the CV curves of LDH-NF and LDH-NF/GNS electrodes, from which a pair of redox peaks with an anodic peak at ~0.4 V and a cathodic peak at ~0.1 V could be observed. This indicated the Faradaic behavior of LDH. The peaks correspond to conversion between the different oxidation states of Ni according to Equation 1 [19]:

$$Ni(OH)_2 + OH^- \leftrightarrow NiOOH + H_2O + e^- \dots (1)$$

In general, the smaller the potential difference between the anodic and cathodic peak potential (ΔE), the better the reversibility in the redox reaction. As shown in Fig. 3a, the LDH-NF electrode (ΔE=315 mV) demonstrated better reversibility than the LDH-NF/GNS electrode (ΔE=360 mV). This was attributed to the larger surface area of the LDH-NF electrode exposed to the electrolyte, which promoted the efficient diffusion of OH$^-$ ions during the redox reactions [41]. Fig. 3b-c showed CV curves of the LDH-NF and LDH-NF/GNS electrodes at different scan rates of 5, 10, 30, 50, 70, and 100 mV s^{-1}, respectively. After increasing the scan rate, the anodic and cathodic peaks in the CV curves shifted towards a positive and negative potential, respectively, leading to a continuous increase in the potential distance between the oxidation and reduction peaks. This indicates the quasi-reversible feature of the redox couples. This observation was ascribed to the ohmic resistance and increasing polarization of the electrode when the electrolyte ions diffused in

12

the porous electrode during the redox reaction at high scan rates [42]. In Fig. 3a-c, compared to the LDH-NF electrode, the CV curve of the LDH-NF/GNS electrode showed lower peak currents and smaller integrated areas, indicating that the LDH-NF/GNS electrode exhibited a lower specific capacity. The results indicated that GNS has a negative effect on the capacitive performance of the electrode. GNS blocked a part of the open-porous structure of LDH (Fig. 2h) and restrained the inner LDH nanoplatelets from the reaction with OH$^-$, and reduced the specific capacitance of the electrode. This finding is in contrast to previous reports of GNS-based powdery composites [19, 32], in which the existence of GNS can serve as a substrate or spacer to prevent aggregation between the neighboring LDH sheets and greatly enhance the electrochemical performance of the electrodes. In addition, Fig. 3d showed the relationships of the cathodic peak current ($I_{p,c}$) to the scan rate (v) of LDH-NF and LDH-NF/GNS electrodes. $I_{p,c}$ increased linearly with $v^{1/2}$, confirming diffusion-control of the electrode process. According to Equation 2 [43],

$$i_p = (2.69 \times 10^5)n^{3/2}AD_o^{1/2}C_o^*v^{1/2} \dots (2)$$

where i_p is the peak current, n is the number of electron transferred, A is the electrode area, D_o is the diffusion coefficient, C_o^* is the reactant concentration, and v is the scan rate. For comparison, the diffusion coefficients ($D_{\text{LDH-NF}}$ and $D_{\text{LDH-NF/GNS}}$) of the LDH-NF and LDH-NF/GNS electrodes were calculated from Equation 3, assuming that both electrodes have the same values of n, A and C_o^*. The diffusion coefficient of the LDH-NF/GNS electrode ($D_{\text{LDH-NF/GNS}}$) was 4.6 times smaller than that of the LDH-NF electrode, indicating the negative effect of the GNS loading on the LDH-NF electrode. This conclusion was further confirmed by the subsequent galvanostatic charge-discharge tests.

$$D_{\text{LDH-NF/GNS}} / D_{\text{LDH-NF}} = [(i_p/v^{1/2})_{\text{LDH-NF/GNS}} / (i_p/v^{1/2})_{\text{LDH-NF}}]^2 = (0.02356/0.05072)^2 = 0.216 \dots (3)$$
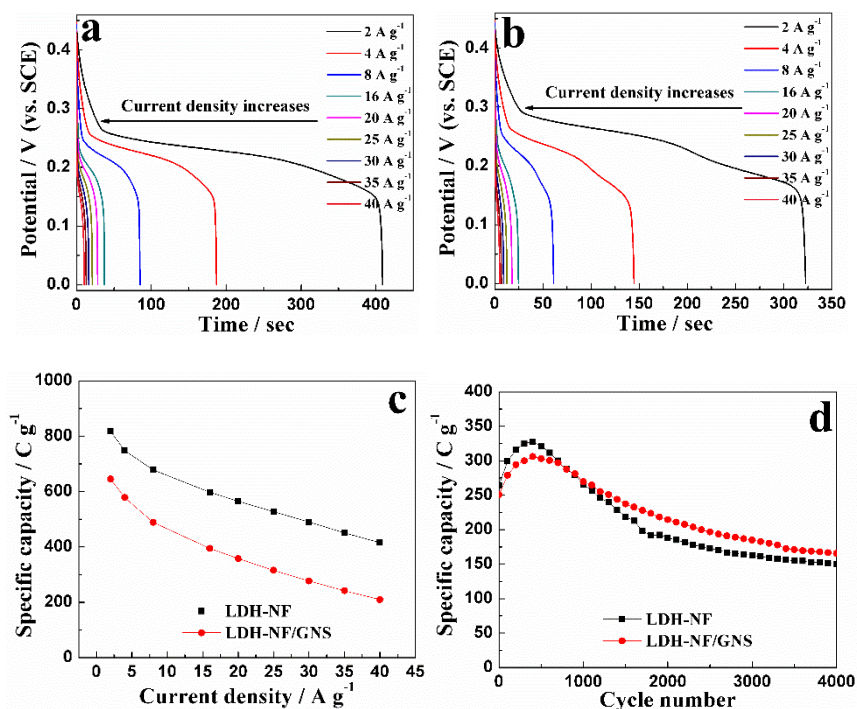
Fig. 4 Discharge curves of (a) LDH-NF and (b) LDH-NF/GNS at different current densities. (c) Specific capacity of LDH-NF and LDH-NF/GNS at different current densities. (d) Cycling stability of the LDH-NF and the LDH-NF/GNS electrodes at 40 A g^{-1}.

As shown in Fig. 4a-b, the discharge measurements of the LDH-NF and LDH-NF/GNS electrodes were carried out between 0-0.45 V (vs. SCE) at different current densities. The definite charge/discharge plateaus can further demonstrate the Faradaic characteristic of electroactive materials due to the quasi-reversible redox reactions at the electrode-electrolyte interface [19]. The calculated capacity (*C*) based on the discharge curves as a function of current density was plotted in Fig. 4c. For the LDH-NF electrode, a high *C* of 817.7 C g^{-1} was obtained at a current density of 2 A g^{-1}, which is higher than that reported for LDH-NF electrodes [24, 31]. The good performance was attributed to the porous nanostructure of LDH on NF. Highly oriented layered thin LDH nanosheets were aligned vertically on NF, leading to the resulting well-defined porous nanostructure of LDH materials [24]. A large number of LDH active sites were exposed to the electrolyte for the Faradaic redox reactions (Equation 1). With the increase in current densities,

14

the capacity decreased, which was caused by the resistance of NiAl-LDH materials and the insufficient Faradaic redox reaction of the active material under higher discharge current densities [19]. The C value of the LDH-NF electrode was reduced to 415.4 C g^{-1} with a retention rate of 50.8% when the current density was increased from 2 to 40 A g^{-1}. For the LDH-NF/GNS electrode, the C value reduced from 645.6 C g^{-1} (at 2 A g^{-1}) to 209.8 C g^{-1} (at 40 A g^{-1}) with a retention rate of 32.5%. Obviously, the specific capacity and high-rate performance of LDH-NF/GNS was worse than those of LDH-NF. Compared to the LDH-NF electrode, a large proportion of the LDH surface was covered with GNS in the LDH-NF/GNS electrode, which reduced the electroactive sites of LDH for the redox reactions and led to a lower specific capacity.
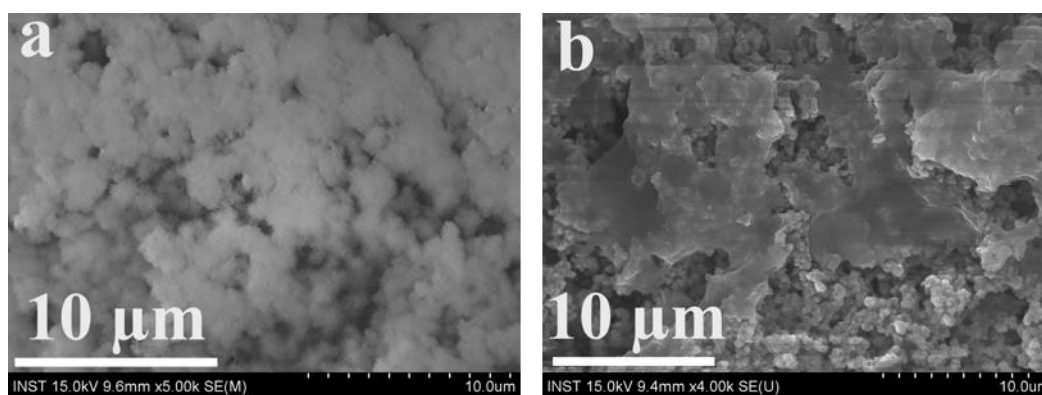

Fig. 5 SEM images of (a) LDH-NF and (b) LDH-NF/GNS after the 4000th cycle test at 40 A g^{-1}.

The high life-cycle stability of the electrode is an important factor in the applications of SCs. The LDH-NF and the LDH-NF/GNS electrodes were tested for 4000 charge/discharge cycles at a high current density of 40 A g^{-1}, as shown in Fig. 4d. The tested cycle number and current density are similar to the conditions of the NiAl-LDH electrodes tested in other studies [19, 24, 32-34, 44]. For both electrodes, a significant increase in specific capacity was observed up to the 400th cycle, which could be attributed to the activation of NiAl-LDH. The two electrodes suffered from a loss of specific capacity during the subsequent 3600th cycle. For the LDH-NF electrode, the C value increased by 23.7% (from 264.3 C g^{-1} to 326.9 C g^{-1}) at a cycle number of 400. It decreased sharply

15

1 in the next 2000 cycles and became stabilized at 150.3 C g^{-1} after the 4000th cycle, which achieved

2 a retention rate of 45.9%. This behavior was attributed to the structural instability of NiAl-LDH in

3 the cycling test [19]. During the continuous prolonged charge/discharge processes, the structure of

4 LDH suffered from considerable degradation, as supported by SEM (Fig. 5a). Compared to Fig.

5 2d, the ball-like assemblies of LDH agglomerated with each other after the 4000 cycle tests at 40

6 A g^{-1}, which decreased the number of redox reactions. Therefore, a drastic reduction of the C value

7 and poor cyclic stability were observed. For the LDH-NF/GNS electrode, the C value increased by

8 22.1% after 400 cycle tests (from 250.6 C g^{-1} to 306 C g^{-1}). Compared to those of LDH-NF, the C

9 value of LDH-NF/GNS decreased more slowly during the 400~4000 cycle tests. After the 4000-

10 cycle test, C was 165.6 C g^{-1} with a retention of 54.1%. As shown in Fig. 5b, the LDH structure

11 was maintained except for the loss of some GNS layers. The flexible GNS film efficiently buffered

12 the volume change in the LDH materials during the long charging and discharging processes. As

13 a result, the structural/crystallographic degradation of the electroactive surface was minimized.

14 Compared to the LDH-NF electrode, the LDH-NF/GNS electrode exhibited better durability and

15 more stable electrochemical performance because of the positive effect of GNS in the electrode.

16 Compared to the previously reported NiAl-LDH-based electrodes (Table S1), the LDH-NF/GNS

17 electrode exhibited very good electrochemical performance in terms of the high specific capacity

18 and stability under high current densities. These results indicated that the LDH-NF/GNS electrode

19 should have potential applications in SCs.

1
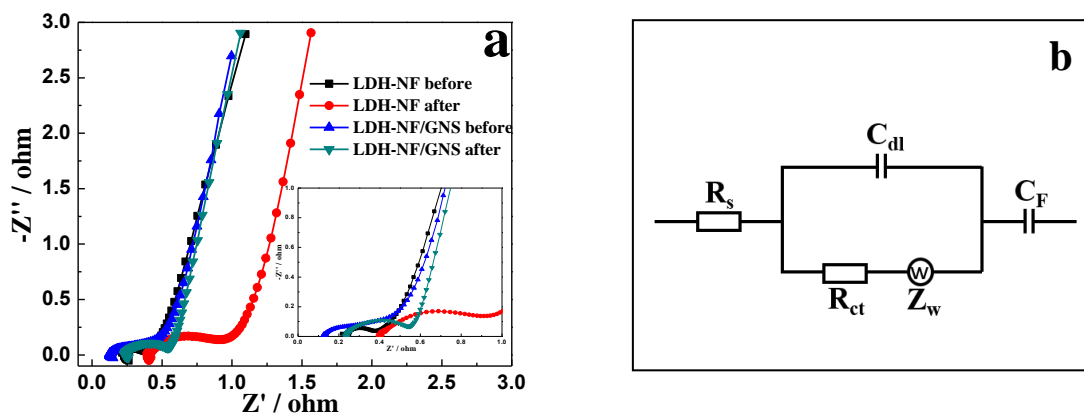
Fig. 6 (a) Nyquist plots of the LDH-NF and the LDH-NF/GNS electrodes before and after the cycling

tests. (b) The electrical equivalent circuit used for fitting the impedance spectra of LDH-NF and LDH-

NF/GNS electrodes.

EIS analysis is commonly used to examine the fundamental behavior of the electrode materials

for SCs. To examine the characteristics of the electrodes, the impedance of the LDH-NF and the

LDH-NF/GNS electrodes before and after the cycling tests were measured, as shown in Fig. 6a.

For each curve, there is a semicircle intersecting the real axis in the high frequency region. The

plot transforms to a vertical line at low frequencies. The semicircle is typical of a RC circuit that

represents a resistance in parallel with a capacitance [45]. In the low frequency region, almost

complete penetration of ions into the surface or pores of the electrode could be allowed. The

vertical line reflects the domination of the capacitive behavior [46]. Fig. 6b shows the proposed

equivalent circuit for the measured impedance data, which involves the internal resistance (R_s),

double-layer capacitance (C_{dl}) and Faradic charge transfer resistance (R_{ct}), a Warburg diffusion

element (Z_w), and pseudocapacitance (C_F) [47-48]. Equation 4 and 5 express the overall impedance,

Z, of the equivalent circuit in Fig. 6b [49]:

$$Z = R_s + \frac{1}{j\omega C_{dl} + \frac{1}{R_{ct} + Z_w}} - j\frac{1}{\omega C_F} \quad \dots (4)$$

17

1
$$Z_w = \frac{W}{\sqrt{j\omega}} \dots (5)$$

2   where j is the imaginary unit, ω is the angular frequency (Hz) and W is the Warburg

3   parameter in units of $\Omega\ s^{-1/2}$. This W parameter is an increasing function of the resistance

4   for electrolyte transport in a porous electrode. At sufficiently high frequencies, the overall

5   impedance can be reduced to Equation 6, corresponding to a locus showing a semicircle

6   that intercepts the real axis at R_s and $R_s + R_{ct}$ in the Nyquist plot [46].

7
$$Z = R_s + \frac{1}{j\omega C_{dl} + \frac{1}{R_{ct}}} \dots (6)$$

8   As a result, in the high frequency region, the intercept of the curve at the real axis (Z') equals

9   R_s, which includes the resistance of the electrolyte, ohmic resistance of the active LDH materials,

10   and contact resistance at the active LDH materials/NF interface. The semicircle, which

11   corresponds to C_{dl} and R_{ct}, displays the charge-transfer process at the working electrode-electrolyte

12   interface. In the low frequency region, the slope of the curve represents the Warburg resistance

13   (Z_w), which is related to electrolyte diffusion in the porous electrode and proton diffusion in the

14   LDH materials. The R_s, C_{dl}, R_{ct}, W, and C_F values were calculated from the complex nonlinear

15   least square fitting of the experimental impedance spectra, as shown in Table 1.

16   **Table 1**. Impedance parameters obtained from the equivalent circuit after fitting

	R_s (Ω)	C_{dl} (F)	R_{ct} (Ω)	W ($\Omega\ s^{-1/2}$)	C_F (F)
LDH-NF (before)	0.245	0.00247	0.134	3.02	5.11
LDH-NF (after)	0.428	0.00482	0.449	3.18	3.69
LDH-NF/GNS (before)	0.145	0.00784	0.179	3.43	4.98
LDH-NF/GNS (after)	0.247	0.00342	0.24	3.47	3.82

17

18   Before the cycling test, the R_s and the R_{ct} values of the LDH-NF electrode were 0.245 Ω and

19   0.134 Ω, respectively. After loading GNS on the LDH-NF electrode, the values of R_s and R_{ct}

18

1   decreased to 0.145 Ω and increased to 0.179 Ω, respectively. For the LDH-NF/GNS electrode, R_s

2   consists of the total ohmic resistance of LDH, NF and GNS. The existence of GNS decreased the

3   internal resistance of the LDH-NF/GNS electrode due to the high conductivity of GNS. The

4   increase in R_{ct} was attributed to some of the open porous structures of LDH being blocked by GNS.

5   Therefore, the electrolyte ions could not effectively reach the LDH surface and react with the

6   active sites. After the 4000th cycle test, the R_s values of the LDH-NF and LDH-NF/GNS electrodes

7   increased, indicating a decrease in conductivity of the electrodes. The R_{ct} values of the electrodes

8   also increased, which might be due to the morphological changes in the LDH (Fig. 5). On the other

9   hand, the R_{ct} of the LDH-NF/GNS electrode was 46.5% smaller than that of the LDH-NF electrode,

10   which was attributed to the positive role of GNS in buffering the volume change in the LDH

11   materials.

12   Before the cycle test, the C_{dl} value of the LDH-NF electrode was lower than that of the LDH-

13   NF/GNS electrode, suggesting that GNS contributed to the charge storage by ion adsorption. For

14   the LDH-NF electrode, the C_{dl} value increased from 2.47 mF to 4.82 mF after 4000 cycles, which

15   was attributed to the better wetting of the electrolyte/electrode interfaces [50]. For the LDH-NF/GNS

16   electrode, however, the C_{dl} value was decreased from 7.84 mF to 3.42 mF after the cycle test,

17   which was due mainly to the loss of GNS of the electrode (as shown in Fig. 5b). Before the cycle

18   test, the W value of the LDH-NF electrode was lower than that of the LDH-NF/GNS electrode,

19   which was attributed to the negative influence of GNS on the active surface of LDH resulting in

20   an increase in resistance for electrolyte transport in a porous electrode. The C_F value of the LDH-

21   NF electrode was slightly higher than that of the LDH-NF/GNS electrode, which was attributed to

22   blockage of the active LDH material by GNS. After the cycle test, for both electrodes, the W values

23   increased and the C_F values decreased. The reduction of C_F was related to the structural stability

19

1   of LDH material. The result indicated that the C_F value of the LDH-NF electrode was slightly

2   lower than that of the LDH-NF/GNS electrode, which further confirmed the positive role of GNS

3   in buffering the structural stability of the LDH material during the charging/discharging tests.

4   To evaluate the performance of a HSC device which utilizes the prepared LDH-NF/GNS as the

5   positive electrode, we prepared porous GNS powders by a facile hydrothermal method, which

6   were then coated on a NF as the negative electrode (GNS-NF). A broad peak at around $2\theta=24.4^o$

7   in the XRD pattern represented an interlayer spacing of 0.36 nm (Fig. S3a). The prepared GNS-

8   NF electrode displayed excellent electric double layer capacitance properties at -1.0 ~ 0.0 V (vs.

9   SCE, Fig. S3b). The C_s of the GNS-NF electrode, which was calculated from its galvanostatic

10   charge-discharge curves (Fig. S3c), reached 214.7 F g^{-1} at 1 A g^{-1} and 143.1 F g^{-1} at 20 A g^{-1} with

11   a good retention rate of 66.7% (Fig. S3d). The results were comparable to those previously reported

12   for graphene-based supercapacitors [51-52]. These electrochemical behaviors showed that prepared

13   GNS-NF electrode could serve as a negative electrode in HSCs.

14

15

20
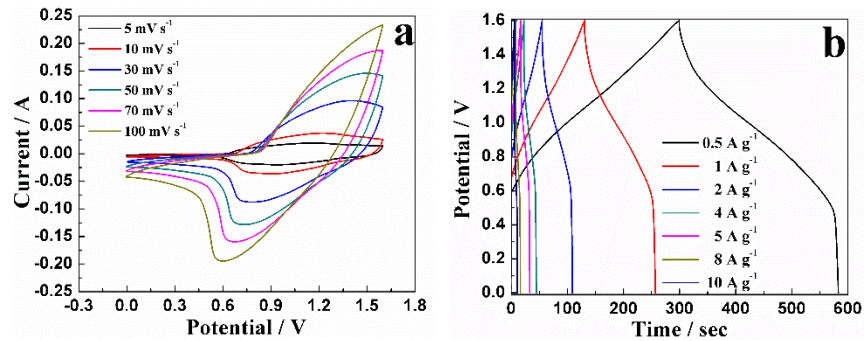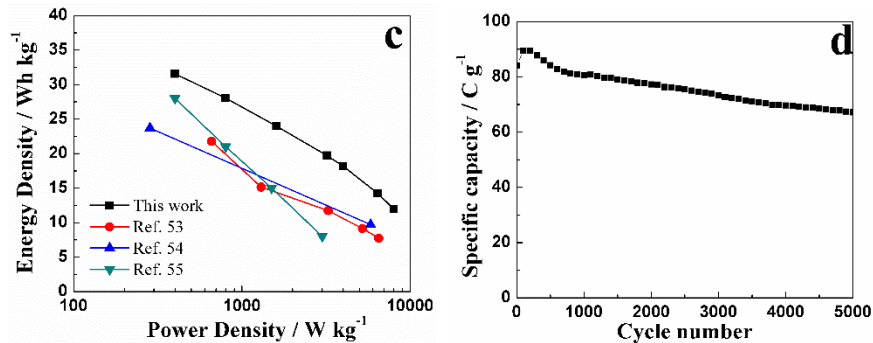
Fig. 7 (a) CV curves of the hybrid supercapacitor LDH-NF/GNS//GNS-NF at different scan rates. (b) Galvanostatic charge-discharge curves of the HSC at different current densities. (c) Ragone plot of the energy and power density at various charge-discharge rates. The values reported for the other devices are given here for comparison. (d) Cycling performance of the HSC at a current density of 5 A g^{-1}.

To evaluate the performance of the LDH-NF/GNS and the GNS-NF electrodes in SC applications, a HSC was fabricated with a new LDH-NF/GNS as the positive electrode and the GNS-NF as the negative electrode. Based on the C or C_s values of the LDH- NF/GNS electrode and the GNS electrode, as well as the principle of charge balance between the electrodes, the mass ratio of LDH-NF/GNS to GNS-NF was controlled at approximately 0.31 in the HSC. Fig. 7a presents a typical CV curves for at various scan rates between 0 and 1.6 V. The CV curves also deviate from a rectangular shape because of the battery-type charge storage mechanism of LDH. With the increase of scan rate from 5 to 100 mV s^{-1}, the shapes of CV curves of the device did not change, implying the good fast charge–discharge properties of the device. Fig. 7b showed the galvanostatic charge-discharge curves, from which the discharge curve was almost symmetrical with its corresponding charge counterpart, demonstrating the excellent electrochemical reversibility and good coulombic efficiency [53]. The specific capacity (C') values were calculated to be 141.9, 126.1, 108, 88.7, 81.8, 64.1 and 53.9 C g^{-1} at current densities of 0.5, 1, 2, 4, 5, 8, and 10 A g^{-1}, respectively (based on the total mass of the active material in the positive and negative electrodes). Based on these C values, the highest energy density of the HSC (Fig. 7c) was calculated to be 31.5 Wh kg^{-1} at a power density of 400 W kg^{-1}. At a high discharge current of 10 A g^{-1}, the energy density was reduced to 12.0 Wh kg^{-1} at a power density of 8000 W kg^{-1}. The results show that the HSC device achieved a higher energy density than the reported devices in literature, such as Co_3O_4-rGO//AC (13.4 Wh kg^{-1} at 180.8 W kg^{-1}) [54], $Ni(OH)_2$@3D Ni//AC (21.8 Wh kg^{-1} at 660 W kg^{-1}) [55], NiCo LDH-Zn_2SnO_4//AC (23.7 Wh kg^{-1} at 284.2 W kg^{-1}) [56] and

1   NiCo$_2$O$_4$@MnO$_2$-NF//AC (28 Wh kg^{-1} at 400 W kg^{-1}) [57]. Moreover, the energy and power densities

2   of the LDH-NF/GNS//GNS-NF outperformed tremendously those of most nickel or cobalt

3   oxides/hydroxides and other typical material-based HSCs (Table S2). The ultrahigh energy density

4   of the device was attributed to the good energy storage ability of the binder-free LDH-NF/GNS

5   electrode. The galvanostatic charge-discharge test was also carried out to evaluate the durability

6   of the as-fabricated HSC with 0 ~1.6 V for 5000 cycles at a current density of 5 A g^{-1}. As shown

7   in Fig. 7d, the specific capacity of the HSC first increased slightly to 89.4 C g^{-1} (~6%) after 100

8   cycles and was stabilized at 67.2 C g^{-1} (with a retention rate of 80%) after 5000 cycles, which was

9   comparable to those of the HSCs [58-59].

10

11   **Conclusions**

12   In conclusion, the loading of GNS on the LDH-NF electrode had both positive and negative

13   effects on the electrochemical performance and the stability of the electrode. Positively, the

14   flexible GNS film could efficiently buffer the volume change of LDH materials during the charge

15   and discharge processes, which resulted in better electrode stability at a high current density of 40

16   A g^{-1}. Negatively, GNS reduced the electroactive surface area of the LDH materials and blocked

17   the path of ion diffusion significantly, thereby hindering the charge transfer resistance between the

18   electrode surface and the electrolyte, leading to a decrease in specific capacity and the rate

19   performance of the electrode. Compared to the other HSC devices reported elsewhere, the

20   proposed HSC (LDH-NF/GNS//GNS-NF) exhibited higher energy and power densities because of

21   the high electrochemical performance of both electrodes. This work highlights the role of GNS on

22   binder-free LDH/NF electrodes for the further development of high-performance SCs.

23

1 **Acknowledgements**

6

References

1. Reddy, M. V.; Rao, G. V. S.;Chowdari, B. V. R. Metal Oxides and Oxysalts as Anode Materials for Li Ion Batteries. *Chemical Reviews* **2013,** *113,* 5364-5457.

2. Jiang, S. P.;Chen, X. Chromium deposition and poisoning of cathodes of solid oxide fuel cells – A review. *Int J Hydrogen Energy* **2014,** *39,* 505-531.

3. Yuan, C.; Yang, L.; Hou, L.; Li, J.; Sun, Y.; Zhang, X.; Shen, L.; Lu, X.; Xiong, S.;Lou, X. W. Flexible Hybrid Paper Made of Monolayer Co3O4 Microsphere Arrays on rGO/CNTs and Their Application in Electrochemical Capacitors. *Adv. Funct. Mater.* **2012,** *22,* 2560-2566.

4. Simon, P.;Gogotsi, Y. Materials for electrochemical capacitors. *Nat. Mater.* **2008,** *7,* 845-854.

5. Huang, Y.-G.; Zhang, X.-H.; Chen, X.-B.; Wang, H.-Q.; Chen, J.-R.; Zhong, X.-X.;Li, Q.-Y. Electrochemical properties of MnO2-deposited TiO2 nanotube arrays 3D composite electrode for supercapacitors. *Int J Hydrogen Energy* **2015,** *40,* 14331-14337.

6. Zhu, Y.; Murali, S.; Stoller, M. D.; Ganesh, K. J.; Cai, W.; Ferreira, P. J.; Pirkle, A.; Wallace, R. M.; Cychosz, K. A.; Thommes, M.; Su, D.; Stach, E. A.;Ruoff, R. S. Carbon-Based Supercapacitors Produced by Activation of Graphene. *Science* **2011,** *332,* 1537-1541.

7. Huang, K.-J.; Wang, L.; Liu, Y.-J.; Liu, Y.-M.; Wang, H.-B.; Gan, T.;Wang, L.-L. Layered MoS2–graphene composites for supercapacitor applications with enhanced capacitive performance. *Int J Hydrogen Energy* **2013,** *38,* 14027-14034.

8. Yuan, C. Z.; Gao, B.; Shen, L. F.; Yang, S. D.; Hao, L.; Lu, X. J.; Zhang, F.; Zhang, L. J.;Zhang, X. G. Hierarchically structured carbon-based composites: Design, synthesis and their application in electrochemical capacitors. *Nanoscale* **2011,** *3,* 529-545.

9. Li, S.;Wang, C.-A. Design and synthesis of hierarchically porous MnO2/carbon hybrids for high performance electrochemical capacitors. *J. Colloid Interf. Sci.* **2015,** *438,* 61-67.

10. Xu, X.; Shen, J.; Li, N.;Ye, M. Microwave-assisted in situ synthesis of cobalt nanoparticles decorated on reduced graphene oxide as promising electrodes for supercapacitors. *Int J Hydrogen Energy* **2015,** *40,* 13003-13013.

11. Cheng, H.; Long, L.; Shu, D.; Wu, J.; Gong, Y.; He, C.; Kang, Z.;Zou, X. The supercapacitive behavior and excellent cycle stability of graphene/MnO2 composite prepared by an electrostatic self-assembly process. *Int J Hydrogen Energy* **2014,** *39,* 16151-16161.

24

12.   Ghasemi, S.; Hosseinzadeh, R.;Jafari, M. MnO2 nanoparticles decorated on electrophoretically deposited graphene nanosheets for high performance supercapacitor. *Int J Hydrogen Energy* **2015,** *40,* 1037-1046.

13.   Yuan, C.; Wu, H. B.; Xie, Y.;Lou, X. W. Mixed Transition-Metal Oxides: Design, Synthesis, and Energy-Related Applications. *Angew Chem Int Ed* **2014,** *53,* 1488-1504.

14.   Ren, X.; Tian, C.; Li, S.; Zhao, Y.;Wang, C.-A. Facile synthesis of tremella-like MnO2 and its application as supercapacitor electrodes. *Frontiers of Materials Science* **2015,** *9,* 234-240.

15.   Aravindan, V.; Cheah, Y. L.; Mak, W. F.; Wee, G.; Chowdari, B. V. R.;Madhavi, S. Fabrication of High Energy-Density Hybrid Supercapacitors Using Electrospun V2O5 Nanofibers with a Self-Supported Carbon Nanotube Network. *ChemPlusChem* **2012,** *77,* 570-575.

16.   Vialat, P.; Mousty, C.; Taviot-Gueho, C.; Renaudin, G.; Martinez, H.; Dupin, J. C.; Elkaim, E.;Leroux, F. High-Performing Monometallic Cobalt Layered Double Hydroxide Supercapacitor with Defined Local Structure. *Adv. Funct. Mater.* **2014,** *24,* 4831-4842.

17.   Li, J.; Shangguan, E.; Nie, M.; Jin, Q.; Zhao, K.; Chang, Z.; Yuan, X.-Z.;Wang, H. Enhanced electrochemical performance of high-density Al-substituted α-nickel hydroxide by a novel anion exchange method using NaCl solution. *Int J Hydrogen Energy* **2015,** *40,* 1852-1858.

18.   Chen, H.; Wang, J. M.; Pan, T.; Xiao, H. M.; Zhang, J. Q.;Cao, C. N. Effects of coprecipitated zinc on the structure and electrochemical performance of Ni/Al-layered double hydroxide. *Int J Hydrogen Energy* **2002,** *27,* 489-496.

19.   Zhang, L. J.; Wang, J.; Zhu, J. J.; Zhang, X. G.; Hui, K. S.;Hui, K. N. 3D porous layered double hydroxides grown on graphene as advanced electrochemical pseudocapacitor materials. *J. Mater. Chem. A* **2013,** *1,* 9046-9053.

20.   Zhang, L.; Zhang, X.; Shen, L.; Gao, B.; Hao, L.; Lu, X.; Zhang, F.; Ding, B.;Yuan, C. Enhanced high-current capacitive behavior of graphene/CoAl-layered double hydroxide composites as electrode material for supercapacitors. *J. Power Sources* **2012,** *199,* 395-401.

21.   Kulkarni, S. B.; Jagadale, A. D.; Kumbhar, V. S.; Bulakhe, R. N.; Joshi, S. S.;Lokhande, C. D. Potentiodynamic deposition of composition influenced Co1−xNix LDHs thin film electrode for redox supercapacitors. *Int J Hydrogen Energy* **2013,** *38,* 4046-4053.

22.   Song, Y.; Wang, J.; Li, Z.; Guan, D.; Mann, T.; Liu, Q.; Zhang, M.;Liu, L. Self-assembled hierarchical porous layered double hydroxides by solvothermal method and their application for capacitors. *Microporous Mesoporous Mater.* **2012,** *148,* 159-165.

23.   Shao, M.; Ning, F.; Zhao, Y.; Zhao, J.; Wei, M.; Evans, D. G.;Duan, X. Core-Shell Layered Double Hydroxide Microspheres with Tunable Interior Architecture for Supercapacitors. *Chem. Mater.* **2012,** *24,* 1192-1197.

24.   Wang, J.; Song, Y.; Li, Z.; Liu, Q.; Zhou, J.; Jing, X.; Zhang, M.;Jiang, Z. In Situ Ni/Al Layered Double Hydroxide and Its Electrochemical Capacitance Performance. *Energy Fuels* **2010,** *24,* 6463-6467.

25.   Sim, H.; Jo, C.; Yu, T.; Lim, E.; Yoon, S.; Lee, J. H.; Yoo, J.; Lee, J.;Lim, B. Reverse Micelle Synthesis of Colloidal Nickel-Manganese Layered Double Hydroxide Nanosheets and Their Pseudocapacitive Properties. *Chemistry-a European Journal* **2014,** *20,* 14880-14884.

26.   Wang, L.; Li, X.; Guo, T.; Yan, X.;Tay, B. K. Three-dimensional Ni(OH)2 nanoflakes/graphene/nickel foam electrode with high rate capability for supercapacitor applications. *Int J Hydrogen Energy* **2014,** *39,* 7876-7884.

27.   Rajeshkhanna, G.; Umeshbabu, E.; Justin, P.;Ranga Rao, G. In situ fabrication of porous festuca scoparia-like Ni0.3Co2.7O4 nanostructures on Ni-foam: An efficient electrode material for supercapacitor applications. *Int J Hydrogen Energy* **2015,** *40,* 12303-12314.

28.   Guan, C.; Liu, J. P.; Cheng, C. W.; Li, H. X.; Li, X. L.; Zhou, W. W.; Zhang, H.;Fan, H. J. Hybrid structure of cobalt monoxide nanowire @ nickel hydroxidenitrate nanoflake aligned on nickel foam for high-rate supercapacitor. *Energy Environ. Sci.* **2011,** *4,* 4496-4499.

29.   Xia, X. H.; Tu, J. P.; Zhang, Y. Q.; Wang, X. L.; Gu, C. D.; Zhao, X. B.;Fan, H. J. High-Quality Metal Oxide Core/Shell Nanowire Arrays on Conductive Substrates for Electrochemical Energy Storage. *ACS Nano* **2012,** *6,* 5531-5538.

30.   Zhao, C.; Wang, X.; Wang, S.; Wang, Y.; Zhao, Y.;Zheng, W. Synthesis of Co(OH)2/graphene/Ni foam nano-electrodes with excellent pseudocapacitive behavior and high cycling stability for supercapacitors. *Int J Hydrogen Energy* **2012,** *37,* 11846-11852.

31.   Wang, B.; Liu, Q.; Qian, Z. Y.; Zhang, X. F.; Wang, J.; Li, Z. S.; Yan, H. J.; Gao, Z.; Zhao, F. B.;Liu, L. H. Two steps in situ structure fabrication of Ni-Al layered double hydroxide on Ni foam and its electrochemical performance for supercapacitors. *J. Power Sources* **2014,** *246,* 747-753.

32.   Gao, Z.; Wang, J.; Li, Z.; Yang, W.; Wang, B.; Hou, M.; He, Y.; Liu, Q.; Mann, T.; Yang, P.; Zhang, M.;Liu, L. Graphene Nanosheet/Ni2+/Al3+ Layered Double-Hydroxide Composite as a Novel Electrode for a Supercapacitor. *Chem. Mater.* **2011,** *23,* 3509-3516.

33.   Memon, J.; Sun, J. H.; Meng, D. L.; Ouyang, W. Z.; Memon, M. A.; Huang, Y.; Yan, S. K.;Geng, J. X. Synthesis of graphene/Ni-Al layered double hydroxide nanowires and their application as an electrode material for supercapacitors. *J. Mater. Chem. A* **2014,** *2,* 5060-5067.

34.   Niu Yulian; Li Ruiyi; Li Zaijun; Fang Yinjun;Liu Junkang High-performance supercapacitors materials prepared via in situ growth of NiAl-layered double hydroxide nanoflakes on well-activated graphene nanosheets. *Electrochim. Acta* **2013,** *94,* 360-366.

35.   Xu, Y. F.; Schwab, M. G.; Strudwick, A. J.; Hennig, I.; Feng, X. L.; Wu, Z. S.;Mullen, K. Screen-Printable Thin Film Supercapacitor Device Utilizing Graphene/Polyaniline Inks. *Advanced Energy Materials* **2013,** *3,* 1035-1040.

36.   Xin, G.; Wang, Y.; Zhang, J.; Jia, S.; Zang, J.;Wang, Y. A self-supporting graphene/MnO2 composite for high-performance supercapacitors. *Int J Hydrogen Energy* **2015,** *40,* 10176-10184.

37.   Chen, Y.; Huang, Z.; Zhang, H.; Chen, Y.; Cheng, Z.; Zhong, Y.; Ye, Y.;Lei, X. Synthesis of the graphene/nickel oxide composite and its electrochemical performance for supercapacitors. *Int J Hydrogen Energy* **2014,** *39,* 16171-16178.

38.   Wang, L.; Wang, D.; Dong, X. Y.; Zhang, Z. J.; Pei, X. F.; Chen, X. J.; Chen, B. A.;Jin, J. A. Layered assembly of graphene oxide and Co-Al layered double hydroxide nanosheets as electrode materials for supercapacitors. *Chem. Commun.* **2011,** *47,* 3556-3558.

39.   Zhou, Y.; Bao, Q. L.; Tang, L. A. L.; Zhong, Y. L.;Loh, K. P. Hydrothermal Dehydration for the "Green" Reduction of Exfoliated Graphene Oxide to Graphene and Demonstration of Tunable Optical Limiting Properties. *Chem. Mater.* **2009,** *21,* 2950-2956.

40.   Chen, H.; Hu, L. F.; Chen, M.; Yan, Y.;Wu, L. M. Nickel- Cobalt Layered Double Hydroxide Nanosheets for High- performance Supercapacitor Electrode Materials. *Adv. Funct. Mater.* **2014,** *24,* 934-942.

41.   Zheng, F. L.; Li, G. R.; Ou, Y. N.; Wang, Z. L.; Su, C. Y.;Tong, Y. X. Synthesis of hierarchical rippled Bi2O3 nanobelts for supercapacitor applications. *Chem. Commun.* **2010,** *46,* 5021-5023.

42.   Meher, S. K.; Justin, P.;Ranga Rao, G. Microwave-Mediated Synthesis for Improved Morphology and Pseudocapacitance Performance of Nickel Oxide. *ACS Appl. Mater. Interfaces* **2011,** *3,* 2063-2073.

43.   Su, L. H.; Zhang, X. G.;Liu, Y. Electrochemical performance of Co-Al layered double hydroxide nanosheets mixed with multiwall carbon nanotubes. *J. Solid State Electrochem.* **2008,** *12,* 1129-1134.

44.   Xu, J.; Gai, S. L.; He, F.; Niu, N.; Gao, P.; Chen, Y. J.;Yang, P. P. A sandwich-type three-dimensional layered double hydroxide nanosheet array/graphene composite: fabrication and high supercapacitor performance. *J. Mater. Chem. A* **2014,** *2,* 1022-1031.

45.   Nian, Y. R.;Teng, H. S. Influence of surface oxides on the impedance behavior of carbonbased electrochemical capacitors. *J. Electroanal. Chem.* **2003,** *540,* 119-127.

46.   Wang, K. P.;Teng, H. S. Structural feature and double-layer capacitive performance of porous carbon powder derived from polyacrylonitrile-based carbon fiber. *J. Electrochem. Soc.* **2007,** *154,* A993-A998.

47.   Ghodbane, O.; Louro, M.; Coustan, L.; Patru, A.;Favier, F. Microstructural and Morphological Effects on Charge Storage Properties in MnO2-Carbon Nanofibers Based Supercapacitors. *J. Electrochem. Soc.* **2013,** *160,* A2315-A2321.

48.   Sen, P.;De, A. Electrochemical performances of poly(3,4-ethylenedioxythiophene)-NiFe2O4 nanocomposite as electrode for supercapacitor. *Electrochim. Acta* **2010,** *55,* 4677-4684.

49.   Huang, C. W.;Teng, H. S. Influence of carbon nanotube grafting on the impedance behavior of activated carbon capacitors. *J. Electrochem. Soc.* **2008,** *155,* A739-A744.

50.   Chaudhari, S.; Bhattacharjya, D.;Yu, J. S. 1-Dimensional porous alpha-Fe2O3 nanorods as high performance electrode material for supercapacitors. *RSC Adv.* **2013,** *3,* 25120-25128.

51.   Wu, Z. S.; Winter, A.; Chen, L.; Sun, Y.; Turchanin, A.; Feng, X. L.;Mullen, K. Three-Dimensional Nitrogen and Boron Co-doped Graphene for High-Performance All-Solid-State Supercapacitors. *Adv. Mater.* **2012,** *24,* 5130-5135.

52.   Yuan, C. Z.; Zhou, L.;Hou, L. R. Facile fabrication of self-supported three-dimensional porous reduced graphene oxide film for electrochemical capacitors. *Materials Letters* **2014,** *124,* 253-255.

53.   Huang, J. C.; Xu, P. P.; Cao, D. X.; Zhou, X. B.; Yang, S. N.; Li, Y. J.;Wang, G. L. Asymmetric supercapacitors based on beta-Ni(OH)(2) nanosheets and activated carbon with high energy density. *J. Power Sources* **2014,** *246,* 371-376.

54.   Yuan, C.; Zhang, L.; Hou, L.; Pang, G.;Oh, W.-C. One-step hydrothermal fabrication of strongly coupled Co3O4 nanosheets-reduced graphene oxide for electrochemical capacitors. *RSC Adv.* **2014,** *4,* 14408-14413.

55.   Su, Y. Z.; Xiao, K.; Li, N.; Liu, Z. Q.;Qiao, S. Z. Amorphous Ni(OH)(2) @ three-dimensional Ni core-shell nanostructures for high capacitance pseudocapacitors and asymmetric supercapacitors. *J. Mater. Chem. A* **2014,** *2,* 13845-13853.

56.   Wang, X.; Sumboja, A.; Lin, M. F.; Yan, J.;Lee, P. S. Enhancing electrochemical reaction sites in nickel-cobalt layered double hydroxides on zinc tin oxide nanowires: a hybrid material for an asymmetric supercapacitor device. *Nanoscale* **2012,** *4,* 7266-7272.

57.   Xu, K. B.; Li, W. Y.; Liu, Q.; Li, B.; Liu, X. J.; An, L.; Chen, Z. G.; Zou, R. J.;Hu, J. Q. Hierarchical mesoporous NiCo2O4@MnO2 core-shell nanowire arrays on nickel foam for aqueous asymmetric supercapacitors. *J. Mater. Chem. A* **2014,** *2,* 4795-4802.

58.   Wang, X.; Yan, C. Y.; Sumboja, A.;Lee, P. S. High performance porous nickel cobalt oxide nanowires for asymmetric supercapacitor. *Nano Energy* **2014,** *3,* 119-126.

59.   Tang, Z.; Tang, C. H.;Gong, H. A High Energy Density Asymmetric Supercapacitor from Nano-architectured Ni(OH)2/Carbon Nanotube Electrodes. *Adv. Funct. Mater.* **2012,** *22,* 1272-1278.